



Constructing an efficient p–n heterojunction photocatalyst $\text{CaFe}_2\text{O}_4/\text{Fe}_2\text{O}_3$ nanocomposite for degradation of methyl orange

Yong Fu¹, Shuangshuang Shan¹, Feng Chen^{2,*}, and Jianshe Hu^{1,*}

¹ Center for Molecular Science and Engineering, College of Science, Northeastern University, Shenyang 110819, People's Republic of China

² Fujian Provincial Key Laboratory of Featured Materials in Biochemical Industry, Fujian Province University Key Laboratory of Green Energy and Environment Catalysis, College of Chemistry and Materials, Ningde Normal University, Ningde 352100, Fujian, People's Republic of China

Received: 28 December 2019

Accepted: 26 August 2020

Published online:
8 September 2020

© Springer Science+Business Media, LLC, part of Springer Nature 2020

ABSTRACT

As the global environment continues to deteriorate, a technology is urgently needed to eliminate the pollution caused by organic dyestuffs in the environment. Although nano- Fe_2O_3 photocatalyst has developed greatly in the field of organic degradation, until now, the degradation efficiency cannot satisfy the demands. This work addresses imperative need by constructing an efficient p–n heterojunction photocatalyst $\text{CaFe}_2\text{O}_4/\text{Fe}_2\text{O}_3$ nanocomposite for improving the methyl orange (MO) degradation efficiency of nano- Fe_2O_3 . Here, the p- $\text{CaFe}_2\text{O}_4/\text{n-Fe}_2\text{O}_3$ nanocomposite was prepared by using the two-step process of hydrothermal method and co-precipitation. The degradation performance of as-developed nanocomposite was tested by altering the experimental parameters including different mass ratio of p- CaFe_2O_4 and n- Fe_2O_3 , photocatalyst dosage, H_2O_2 volume, initial concentration of MO and pH, and degradation intermediates were analyzed by HPLC and MS. Experimental results indicated the degradation efficiency of prepared sample was up to 99% at 60 min under the optimized conditions, meanwhile, it showed high removal ability after five repeated utilizations. Furthermore, the photocatalytic mechanism was systematically explored based on degradation intermediates. Overall, the nanocomposite photocatalyst was not only designed with using cheap and abundant materials via a simple route, but also exhibited outstanding photocatalytic activity, which will supply a new possibility to effectively deal with the large volume organic pollutants from the textile industry.

Address correspondence to E-mail: chenfeng710828@163.com; hujs@mail.neu.edu.cn

1 Introduction

Nowadays, the global industrial production of dyes can reach 7×10^8 kg per year, and a great deal of wastewater is generated at the same time. However, until now, there is no an effective and easy method to deal with the industrial pollutions [1, 2]. These wastewater discharged into ecosystems will continue to consume the dissolved oxygen in water, resulting in the death of a large number of aquatic organisms. What's worse, because of high genotoxicity and endocrine disrupting potency, dyestuffs can directly affect human health through the contamination of drinking water [3]. The dyes are divided into many types, and the azo dyes are the most frequently used. Methyl orange (MO), as one of azo dyes, has been widely used in printing and photographic industries, and it has a strong carcinogenicity and serious dangers on human health [4]. Therefore, it is urgent to develop a technology to deal with MO in water.

Currently, conventional treatment methods of dye wastewater such as adsorption [5] chemical precipitation [6] are commonly used. These methods can decrease the pollutants concentration in water, but they only transfer contaminants to other substances, which do not completely eliminate or degrade the organic pollutants [7]. Other wastewater treatment technologies, such as sedimentation, chemical oxidation, and biotechnology, always require complex operations and high costs; meanwhile, they also generate additional contaminants [8]. In contrast to the conventional technologies, photocatalytic degradation has become a promising technique to remove dye pollution based on its unique advantages, such as simplicity, high efficiency, environmental friendliness, and economic feasibility [9–11].

TiO₂ [12–14], WO₃ [15], and ZnO [16] have been widely applied in the field of pollutants degradation due to their high photocatalytic activity and excellent chemical stability. Photocatalytic performance is a process of photoelectron capture and inactivation. In the process, some factors would promote the recombination of photoelectron/hole pair, because the photoelectrons are unstable in the excited state, which reduces the photoluminescence efficiency and further lower photocatalytic efficiency [17]. It is still a challenge to stop the recombination of electron/hole pair and improve the range of spectral response and photoluminescence efficiency.

In recent years, creating heterojunction has become a new approach to reduce the photocatalytic photoelectron–hole recombination based on the internal electric field induced from band bending facilitates the photogenerated charge carrier separation [18, 19]. So far, n–n-type heterojunction materials such as TiO₂/Sb₂S₃ [20], ZnO/ α -Fe₂O₃ [21], MoS₂/GaAs [22], and mpg-C₃N₄/SnCoS₄ [23] have been commonly studied. However, compared with the n–n-type heterojunction, p–n-type heterojunction is different in the working mechanism and more beneficial for the separation of the electrons and holes in the opposite direction, due to the built-in electrical potential in the space charge region transferred from the n-type side to the p-type side in the heterojunction structure [24, 25]. However, due to the scarcity of p-type semiconductor oxides, composite photocatalysts with p–n heterojunction have been rarely studied.

Herein, we aimed to fabricate a p–n heterojunction electrode between p-CaFe₂O₄ and n-Fe₂O₃. α -Fe₂O₃ is selected as a n-type photocatalyst owing to the excellent properties including narrow band gap ($E_g = 2.1$ eV), low-cost synthesis, and product free of pollution [26, 27]. Currently, there are many researchers devoting to the combination of Fe₂O₃ in different nano-species for the photocatalytic degradation of pollutants [28, 29]. In addition, ferrite nanomaterials are important semiconductor materials and applied in various degradation of organic pollutants [30]. Spinel ferrites can be generalized as AFe₂O₄ (A can be Mn, Mg, Ni, Zn, etc.) where A and Fe are metal cations which occupy tetrahedral and the octahedral sites, respectively [31, 32]. There have been many studies of high-efficiency n-type ferrite, for example, n-ZnFe₂O₄, whereas there are few studies on p-type semiconductors. The CaFe₂O₄ is a p-type oxide semiconductor and exhibits good properties such as low mass transfer resistance, low toxicity, easy preparation and narrow bandgap (about 1.9 eV) [33, 34]. Currently, the CaFe₂O₄ has been widely applied to fabricate the p–n heterojunction electrode such as CaFe₂O₄/TiO₂ [35], CaFe₂O₄/ZnO [36], CaFe₂O₄/TaON [37] and CaFe₂O₄/MgFe₂O₄ [38].

However, there is little research reported on the photocatalytic degradation of organic pollutant using p-CaFe₂O₄ and n-Fe₂O₃ as a heterojunction photocatalyst, so the construction of a p–n-type photocatalyst with p-CaFe₂O₄ and n-Fe₂O₃ is of great significance. In this study, we prepared a p–n

heterojunction photocatalyst by introducing the n-Fe₂O₃ overlayer onto p-CaFe₂O₄, and the effects of the different mass ratio of p-CaFe₂O₄ and n-Fe₂O₃, the composite photocatalyst dosage, H₂O₂, and the initial concentration of MO and pH on degradation were discussed systematically. In addition, the main degradation products of MO were detected with HPLC and MS, and the photocatalytic reaction mechanism and the degradation pathway of MO were investigated. This fundamental study will provide a new insight for the photocatalytic degradation of dyes using p-CaFe₂O₄/n-Fe₂O₃ nanocomposite to maintain their concentration within permissible limits.

2 Experimental methods

2.1 Materials

FeCl₃·6H₂O was purchased from Sinopharm Chemical Reagent Co., Ltd (Shanghai, China). Sodium dodecyl sulfate, sodium hydroxide, ethanol, and Fe(NO₃)₃·9H₂O were purchased from Damao Chemical Agent Company (Tianjin, China). Ca(NO₃)₂·4H₂O was purchased from Tianjin Bodi Chemical Co., Ltd (Tianjin, China). Potassium carbonate was purchased from Shenyang Xinxing Chemical Reagent plant (Shenyang, China). 30% Hydrogen peroxide and methyl orange were purchased from Shenyang Li Cheng reagent plant (Shenyang, China). All other solvents and reagents used were purified by standard methods.

2.2 Preparation of p-CaFe₂O₄/n-Fe₂O₃ nanocomposite

2.2.1 Preparation of α-Fe₂O₃

1.0 g of Sodium dodecyl sulfate was dissolved in 50 mL of deionized water in a flask, then 3.0 g of FeCl₃·6H₂O was added to above solution and stirred for 15 min. After that, a solution containing 1.2 g of NaOH and 15 mL of deionized water was added dropwise to the mixture solution under stirring, and the system was stirred for 30 min, which formed a reaction precursor solution. Then, the precursor solution was diverted into a stainless steel autoclave at 200 °C for 24 h and then cooled to room temperature. Finally, the product was centrifuged and

washed with deionized water and ethanol and dried in the oven at 80 °C for 20 h. Fig. S1 (scheme 1) and Fig. S2 show schematic of the synthesis method and reactions of the n-Fe₂O₃.

2.2.2 Preparation of p-CaFe₂O₄/n-Fe₂O₃

The different mass ratios of n-Fe₂O₃ and p-CaFe₂O₄ including 1: 0.25, 1: 0.5, 1: 0.75, 1: 1, 1: 1.25, 1: 1.5, 1: 1.75, and 1: 2 were prepared in our work. Here, the mass ratio of n-Fe₂O₃ and p-CaFe₂O₄ (1:1.25) as an example was described as follows. Firstly, a NaOH solution (1.12 g NaOH, 10 mL deionized water) was added dropwise to the Fe(NO₃)₃ solution (4.68 Fe(NO₃)₃·9H₂O and 10 mL deionized water) under stirring, and the mixed solution was still stirred for 15 min. After that, the reddish brown colloidal compound **1** was obtained. Secondly, a K₂CO₃ solution (0.80 g K₂CO₃ and 10 mL deionized water) was added dropwise to a solution of a Ca(NO₃)₂ solution (1.37 g Ca(NO₃)₂·9H₂O, 10 mL deionized water) under stirring, and the white flocculent compound **2** was obtained. Subsequently, the compound **1** was added to the compound **2**, and afterwards, the mixture was stirred for 30 min. Then, 1 g α-Fe₂O₃ was added to the mixture, and the precursor was diverted into a stainless steel autoclave at 95 °C for 6 h, centrifuged and dried. Finally, the Fe₂O₃/CaFe₂O₄ composite particles were obtained after the precursor calcination at 800 °C for 4 h in the muffle furnace. Fig. S1 (scheme 2) and Fig. S2 show schematic of the synthesis method of p-CaFe₂O₄/n-Fe₂O₃ and reactions of the p-CaFe₂O₄.

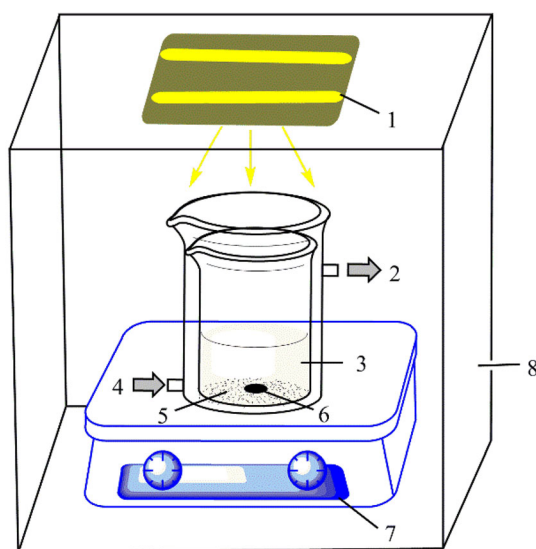
2.3 Characterization

X-ray diffraction (XRD) was performed to determine the crystal structure of samples by using a DMAX-3A Rigaku XRD powder diffractometer (Bruker, German) with a nickel-filtered Cu-Kα radiation at a scan rate of 0.02 s⁻¹ from 2θ = 10 to 80°. The morphologies of the crystals were observed by scanning electron microscope (SEM, JEOL 6500F, Japan). FT-IR spectra were measured on a PerkinElmer spectrum One (B) spectrometer (PerkinElmer, Foster City, CA, USA). The phase transition temperature was determined by a Netzsch 204 differential scanning calorimetry (DSC, Netzsch, Hanau, Germany) equipped with a cooling system at a heating and cooling rate of 10 °C/min in a nitrogen atmosphere.

Thermal decomposition temperature was investigated under nitrogen atmosphere with a Netzsch 209C thermogravimetric analysis (TGA, Hanau, Germany) at a heating rate of 20 °C/min. The absorption wavelength was measured using a UV–Vis spectrophotometer (TU-1901, Beijing Purkinje General Instrument Co., Ltd. China) with a wavelength range of 190–600 nm. The degradation products of methyl orange were analyzed by high performance liquid chromatography (HPLC, Waters 2695, USA) and mass spectrometry (MS, LCQ-FIEET, USA). Other instruments are listed as follows: solid phase extraction instrument (Dongkang Technology Co., Ltd.) and high pressure mercury lamp (GGZ250, Shanghai Jiguang special lighting electrical appliance factory).

2.4 Photodegradation experiments

Photodegradation experiments of MO were investigated by using the high pressure mercury lamp (250 W) with a light source emitting around 365 nm, and the reactor of photocatalysis for MO is shown in Fig. 1. The distance between the light source and the bottom of the reactor was about 20 cm, and the device was cooled by flowing water to ensure that the reaction temperature was fixed, and the detailed experimental procedure was as follows. Firstly, the photocatalyst (0–80 mg) and the 30% H₂O₂ (0–50 μL)



1-UV lamp 2-Cooling water outlet 3-MO solution 4-Cooling water inlet
5-n-Fe₂O₃/p-CaFe₂O₄ 6-Rotor 7-Magnetic stirrer 8-Black box

Fig. 1 Reactor of photocatalysis for MO

were mixed with the MO standard solution (100 mL, 25–100 mg/L) under magnetically stirring, then the solution pH was adjusted with dilute HCl or NaOH solution. Secondly, the mixture was placed in a photoreactor and stirred at about 25 °C. During the experiment, the suspension was collected in an interval time, and a small amount of Na₂SO₃ was added to the suspension to stop the reaction. The clear solution was obtained by centrifugation and measured using UV–Vis spectrophotometer to evaluate the degradation efficiency of MO.

2.5 HPLC and MS

In order to further explore the degradation process of MO, the MO degradation products were measured by HPLC. The measurement conditions were performed as follows. The HPLC system was consisted of an automatic sample injector (injection volume, 10 μL). The mobile phase was an aqueous solution containing acetonitrile (acetonitrile/water = 40:60). The flow rate, UV detection wavelength, and column temperature were set as 60 mL/min, 464 nm and 30 °C, respectively.

The degradation products of methyl orange were preliminarily detected based on HPLC, and further confirmed by MS. The experimental conditions containing ionization source, ionization mode, capillary temperature, capillary voltage, and molecular weight scan range were selected as follows: electrospray (ESI), negative ion mode, 300 °C, 4.0 kV, and 50–1000, respectively.

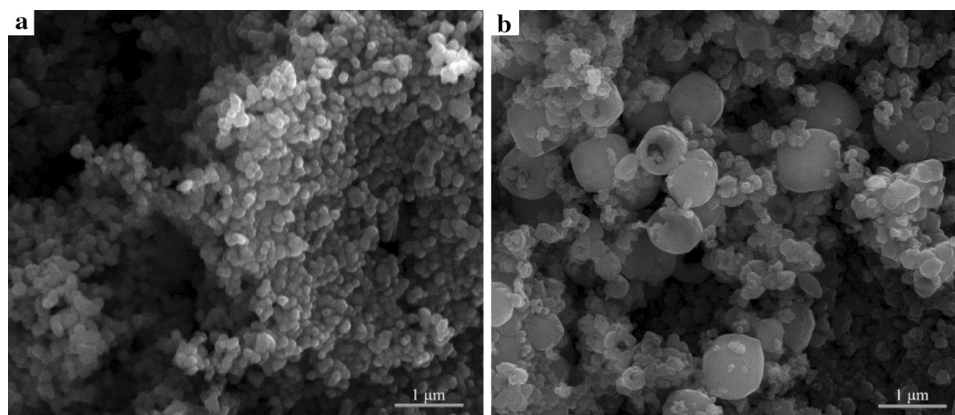
3 Results and discussion

3.1 Characterization of morphology, structure and compositional properties

3.1.1 SEM, TEM and DLS analysis

The SEM micrographs of the n-Fe₂O₃ and p-CaFe₂O₄/n-Fe₂O₃ are shown in Fig. 2. It can be seen that the α-Fe₂O₃ is a spherical nanoparticle with mean sizes of about 20–40 nm; meanwhile, Fig. 2b also exhibits the p-CaFe₂O₄ is formed with bigger spherical diameter (0.1–3 μm) and disperse over the particle of n-Fe₂O₃. Fig. S3 shows the microstructures of the n-Fe₂O₃ and p-CaFe₂O₄/n-Fe₂O₃ via TEM, which indicates the particles are mainly spherical in shape

Fig. 2 **a** SEM pictures of α - Fe_2O_3 and **b** n- Fe_2O_3 /p- CaFe_2O_4



and accompanied by some irregular particles. Furthermore, the particle size and distribution of n- Fe_2O_3 and p- CaFe_2O_4 /n- Fe_2O_3 is shown in Table S1 and Fig. S4. From Table S1, it can be seen that the average diameter of n- Fe_2O_3 is consistent with the results of SEM and TEM analysis, and average diameter of p- CaFe_2O_4 is approximately 2374 nm on average.

3.1.2 XRD analysis

The XRD patterns of α - Fe_2O_3 , CaFe_2O_4 , and p- CaFe_2O_4 /n- Fe_2O_3 with 2θ range of 15° – 80° are shown in Fig. 3a. It can be seen from Fig. 3a that the diffraction peaks in the patterns are consistent with the JCPDS data of α - Fe_2O_3 (JCPDS 84-0311) and CaFe_2O_4 (JCPDS 65-1333). The diffraction peaks of two products are sharp and intense, and no impurity peaks are observed, which indicates the well-crystalline and high-purity of the products. Compared to the spectrum of the composite photocatalyst with the standard card of Fe_2O_3 and CaFe_2O_4 , it can be seen that the CaFe_2O_4 was successfully prepared, and the results were consistent with the experimental design.

3.1.3 FT-IR analysis

The typical FT-IR spectra of α - Fe_2O_3 and p- CaFe_2O_4 /n- Fe_2O_3 are presented in Fig. 3b. The peak at 570 cm^{-1} belongs to the Fe–O bonds, indicating the formation of iron oxide crystals. The short band at 1628 cm^{-1} and a broad band at 3450 cm^{-1} can be attributed to the bending vibration and stretching peak of O–H from absorbed water, respectively. Except for the characteristic peaks of the α - Fe_2O_3 , a new peak at 1400 cm^{-1} can be assigned to the Fe–Ca

stretching vibration of CaFe_2O_4 , demonstrating the presence of CaFe_2O_4 in the composite photocatalyst.

3.1.4 DSC analysis

Figure 3c shows the DSC curve of α - Fe_2O_3 . As seen, there is no obvious endothermic peak at 180 – 200°C , indicating that all the precursor FeOOH has been converted into Fe_2O_3 . In addition, no endothermic peak of the surfactant is observed, confirming that the Fe_2O_3 is pure. Figure 3d shows the DSC curve of p- CaFe_2O_4 /n- Fe_2O_3 , it can be seen that the curve is very smooth and has no obvious endothermic peak, indicating that the products are pure. The results are in good consistent with the XRD and FT-IR results.

3.1.5 XPS analysis

The XPS analysis of the p- CaFe_2O_4 /n- Fe_2O_3 is showed in Fig. S5. Fig. S5(a) gives the full-scan survey XPS spectra of p- CaFe_2O_4 /n- Fe_2O_3 , which reveals the presence of Ca, Fe, and O signals. Deconvolution of the Ca signal (Fig. S5(b)) shows two peaks with binding energies at 350.46 and 346.94 eV, corresponding to Ca $2p_{1/2}$ and $2p_{3/2}$ peaks, respectively, which is consistent with the valence of Ca(II) in the CaFe_2O_4 compound as previously reported. Fig. S5(c) presents the deconvolution of Fe, and the two peaks locating at 724.45 and 710.90 belong to the Fe $2p_{1/2}$ and Fe $2p_{3/2}$, respectively. Fig. S5(d) gives the O 1s signal with two peaks at 529.60 and 531.60 eV, which correspond to lattice oxygen and the latter corresponds to hydroxyl groups at the surface.

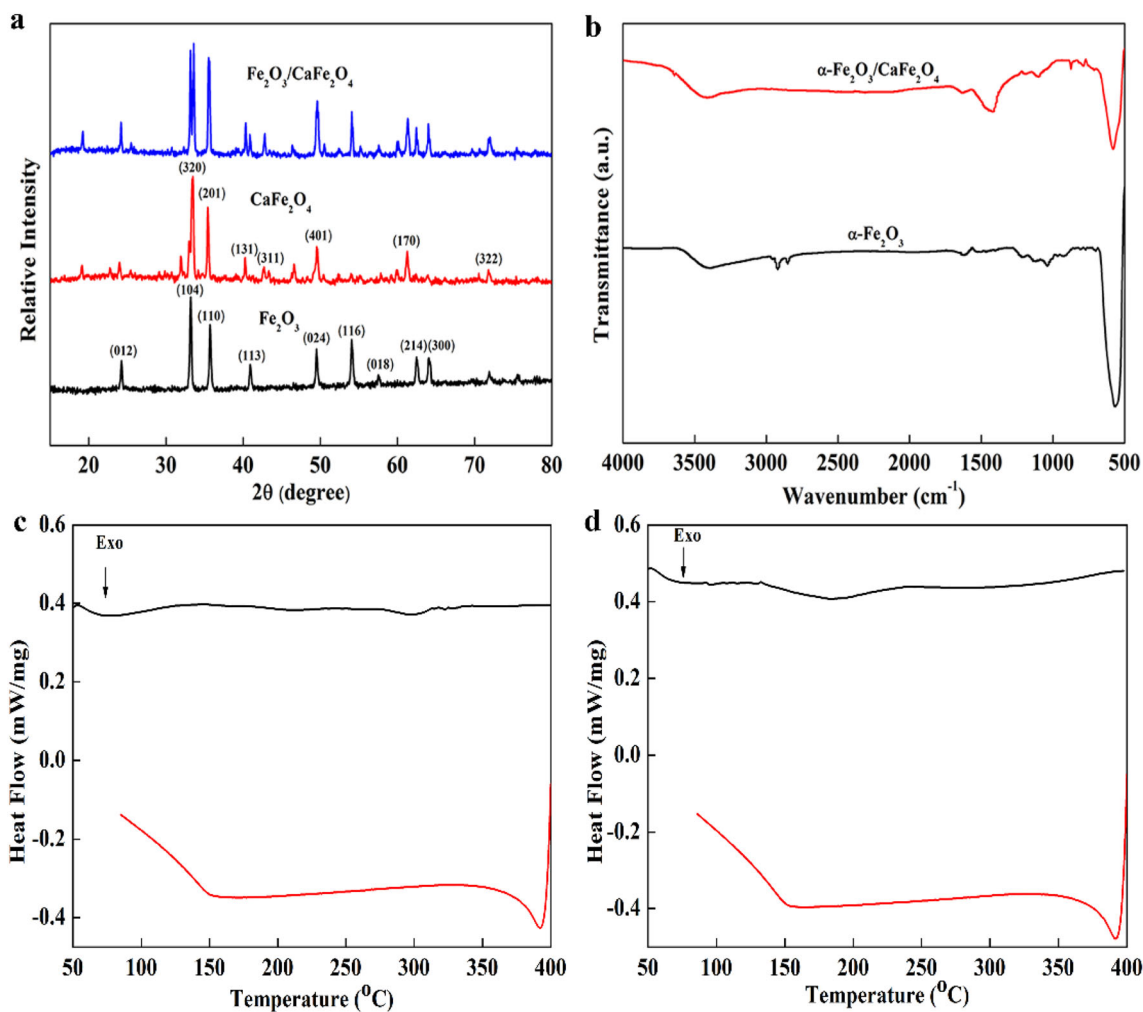


Fig. 3 **a** XRD patterns of α -Fe₂O₃, CaFe₂O₄ and n-Fe₂O₃/p-CaFe₂O₄ powders, **b** FT-IR spectra of α -Fe₂O₃ and n-Fe₂O₃/p-CaFe₂O₄, **c** DSC curves of α -Fe₂O₃, **d** DSC curves of n-Fe₂O₃/p-CaFe₂O₄

3.2 Establishment of the standard curve

Figure S6(a) presents the UV–Vis spectra of the standard MO solutions (1, 2, 3, 5, and 10 mg/L) scanned at 190–600 nm. According to Fig. S6(a), the standard relationship curve of absorbance and the MO concentration was obtained based on the characteristic absorption wavelength of 464 nm, and it was shown in Fig. S6(b). From the standard curve, the absorbance of solution was linear with the MO concentration and the regression equation (Eq. 1) was obtained from the standard curve. The concentration of MO at regular time intervals can be calculated by the intensity of absorption band, and the degradation efficiency can be obtained according to the following expression (Eq. 2).

$$A = 0.0693c + 0.0080 \quad R^2 = 0.9999 \quad (1)$$

$$K = \frac{A_0 - A_t}{A_0} \times 100\% \quad (2)$$

A represents absorbance, A_0 and A_t are the absorbance of the initial solution and the solution at the time t , c is the MO concentration (mg/L), and K is the degradation rate.

3.3 Photocatalytic activity

3.3.1 Effect of different mass ratio of n-Fe₂O₃ and p-CaFe₂O₄ on degradation

MO degradation rate based on the effect of different mass ratio of n-Fe₂O₃ and p-CaFe₂O₄ is exhibited in Fig. 4. As seen from Fig. 4, the degradation rate of the

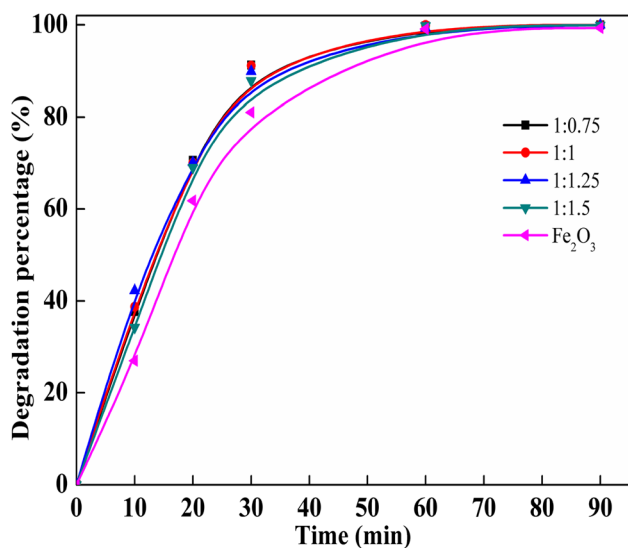


Fig. 4 Effect of different mass ratio of n-Fe₂O₃ and p-CaFe₂O₄ on degradation

composite photocatalyst was higher than that of pure n-Fe₂O₃, and the catalytic efficiency slowly increased with the mass ratio changing from 1:0.75 to 1:1.25, indicating that the p–n heterojunction effect played a major role in the photocatalytic process. However, catalytic efficiency slowly declined when the ratio exceeded 1:1.25, because the photoelectric effect of p-CaFe₂O₄ was much weaker than n-Fe₂O₃, the catalytic effect decreased when CaFe₂O₄ dominated. As a result, the optimum mass ratio of n-Fe₂O₃ and p-CaFe₂O₄ was 1:1.25.

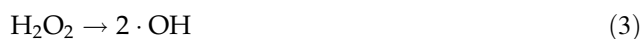
3.3.2 Effect of the photocatalyst dosage on degradation

Figure 5a displays the effect of catalyst dosage on photocatalytic activity of MO. From Fig. 5a, the amount of photocatalyst had a certain effect on the catalytic efficiency, which could be explained as follows: with an increase of the catalyst dosage in the reaction system, the specific surface area of the catalyst and the number of electron–hole pairs increased, which resulted in the improvement the corresponding photocatalytic efficiency. However, because of the color of photocatalyst, the dispersion of the excessive photocatalyst in the solution would impede the spread of light in the suspension system, which would result in the light scattering degree increase and the amount of transmitted light decrease, and finally caused that the measured degradation rate was lower than the actual value. At 10 min, the degradation rate with the catalyst dosage of 10 mg,

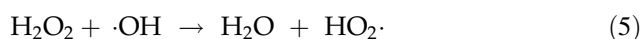
shown in Fig. 5a, was the best and could reach up to 50%. In addition, the degradation rate of the system H₂O₂/UV without the catalyst was the lowest among the series of degradation experiments.

3.3.3 Effect of H₂O₂ volume on degradation

Figure 5b depicts the photocatalytic performance of p-CaFe₂O₄/n-Fe₂O₃ with different H₂O₂ volume. As shown in Fig. 5b, the degradation efficiency of MO without H₂O₂ was very low and the degradation rate at 90 min was less than 10%, but the degradation rate of MO was significantly facilitated with the increase of H₂O₂ volume from 0 to 30 μL, indicating that the H₂O₂ concentration played an important role in the degradation performance of p-CaFe₂O₄/n-Fe₂O₃, which could be attributed to that H₂O₂ could be photolyzed to produce hydroxyl group under light irradiation, and H₂O₂ could capture electrons and inhibit the phenomenon of photoelectron–hole recombination, leading to an increase of the photocatalytic efficiency according to Eqs. (3–4) [39].



However, further increasing H₂O₂ volume, the degradation rate could maintain a constant value and the degradation rate at H₂O₂ volume of 80 μL was very close to that at H₂O₂ dosage of 30 μL. Maybe the possible reason was that the generation of ·OH was suppressed according to Eqs. (5–6) [40, 41], when H₂O₂ was excessive. Therefore, the H₂O₂ dosage of 30 μL was an optimal dosage in this study.



3.3.4 Effect of the initial MO concentration on degradation

The effect of the initial MO concentration on the degradation efficiency was explored. Figure 5c shows the MO degradation curves with different initial MO concentration from 25 to 100 mg/L. When the initial concentration was 25 mg/L, the MO degradation rate could reach 90% at 10 min. However, when the initial concentration was increased to 100 mg/L, the MO degradation rate was less than 10% at 30 min. The results could be explained as follows: the

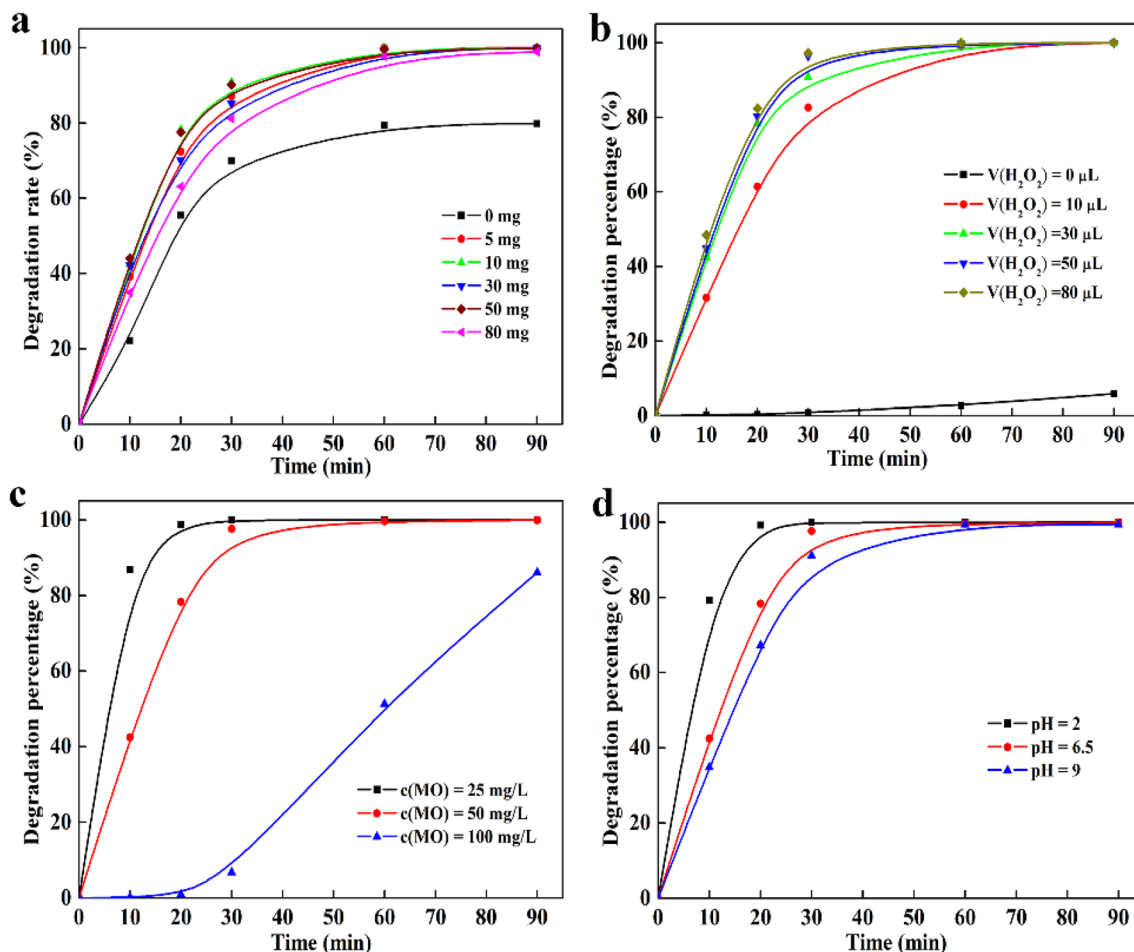


Fig. 5 **a** Effect of n-Fe₂O₃/p-CaFe₂O₄ dosage on MO degradation (50 mg/L MO, 100 mL; 30% H₂O₂, 30 μL; pH, 6.5; temperature, 25 °C). **b** Effect of H₂O₂ dosage on MO degradation (n-Fe₂O₃/p-CaFe₂O₄, 10 mg; 50 mg/L MO, 100 mL; pH, 6.5; temperature, 25 °C). **c** Effect of initial MO concentration on MO degradation

(n-Fe₂O₃/p-CaFe₂O₄, 10 mg; 30% H₂O₂, 30 μL; pH, 6.5; temperature, 25 °C). **d** Effect of the solution pH on MO degradation (n-Fe₂O₃/p-CaFe₂O₄, 10 mg; 50 mg/L MO, 100 mL; 30% H₂O₂, 30 μL; temperature, 25 °C)

photocatalytic degradation of organics was believed to be that the charge transfer process occurred between organics adsorbed on the catalyst surface and the active groups generated by the light irradiation (electron–hole pairs, ·OH, etc.). With the initial MO concentration increase, the amount of light reaching the surface of the semiconductor catalyst also decreased, leading to the number of active groups reduce [42]. Considering the photocatalytic degradation efficiency and economic benefits, the optimum initial MO concentration was chosen as 50 mg/L.

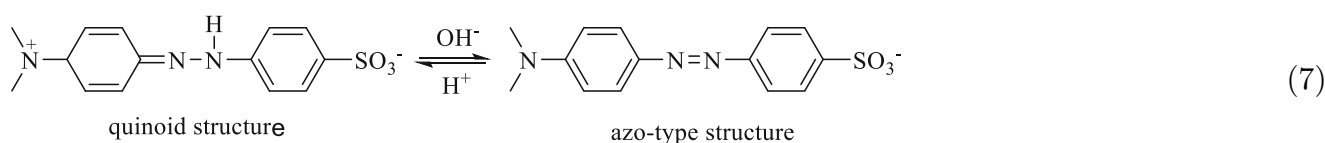
3.3.5 Effect of pH on degradation

As shown in Fig. 5d, the degradation rate increased with the pH value of MO solution decrease, and the acidic environment was more favorable for the MO degradation. The superior activity of p-CaFe₂O₄/n-Fe₂O₃ in acidic solutions could be explained as follows: First, according to Eq. 7, the quinoid structure of MO without stable N=N bonds was easily degraded under acidic conditions. However, MO was an azo-type structure in alkaline conditions, so the degradation rate became slower. Secondly, according to the zeta potentials of p-CaFe₂O₄/n-Fe₂O₃ in acidic solution (Table S2), n-Fe₂O₃ surface was positively charged and inclined to absorb negatively charged MO molecules, which would accelerate the

degradation reaction. Meanwhile, and with the pH decreasing from 2 to 6.5, the Zeta potentials of p-CaFe₂O₄/n-Fe₂O₃ decreased from 22.1 to 2.78 mV. In addition, H₂O₂ in alkaline solutions was unstable and could decompose into water, which would reduce the amount of ·OH [43]. Degradation rate was faster under lower acidic conditions; however, considering that the pH of industrial wastewater was closer to 6.5, the optimum pH for MO degradation in the experiments was still chosen as 6.5.

close to be separated. Therefore, in order to study the mechanism of degradation, the corresponding degradation intermediates of MO were further identified by MS.

Figures S13 and S14 show the mass spectrogram of products for 10 min and 60 min. As shown in Fig. S13, the fragment ions of *m/z* 328, 314, 306, and 292 appeared in the spectra of 10 min degradation, which matched the MO, C₁₃H₁₂O₃N₃SNa, C₁₄H₁₆O₃N₃S⁻, and C₁₃H₁₂O₃N₃S⁻. The fragment ions *m/z* of



3.4 Photocatalyst regeneration

The recyclability of nanocomposites and the steady degradation efficiency of dyes are important indicators to assess an excellent photocatalyst in practical remove process. Fig. S7 shows the degradation efficiency at different regeneration cycles. Although the degradation efficiency gradually decreased after each cycle due to loss of p-CaFe₂O₄/n-Fe₂O₃ in the recycling process, it still reached to 76.67% in the fifth cycle; therefore, the p-CaFe₂O₄/n-Fe₂O₃ exhibited good reusability in the regeneration experiments.

3.5 Photocatalytic degradation reaction mechanism

In order to explore the degradation process of MO, the type and retention time of MO degradation products were analyzed by liquid chromatography. Figs. S8–S12 shows the HPLC chromatograms of MO solution with the corresponding degradation time of 0, 20, 40, 60, and 90 min. With the gradual degradation, the characteristic peak of MO gradually split into two parts and the ratio of the peak value between the left and right peak gradually increased, indicating that the substance corresponding to the right peak was gradually transformed into that corresponding to the left peak. However, no other peak was observed in the liquid chromatography, because the polarities of some individual products were too

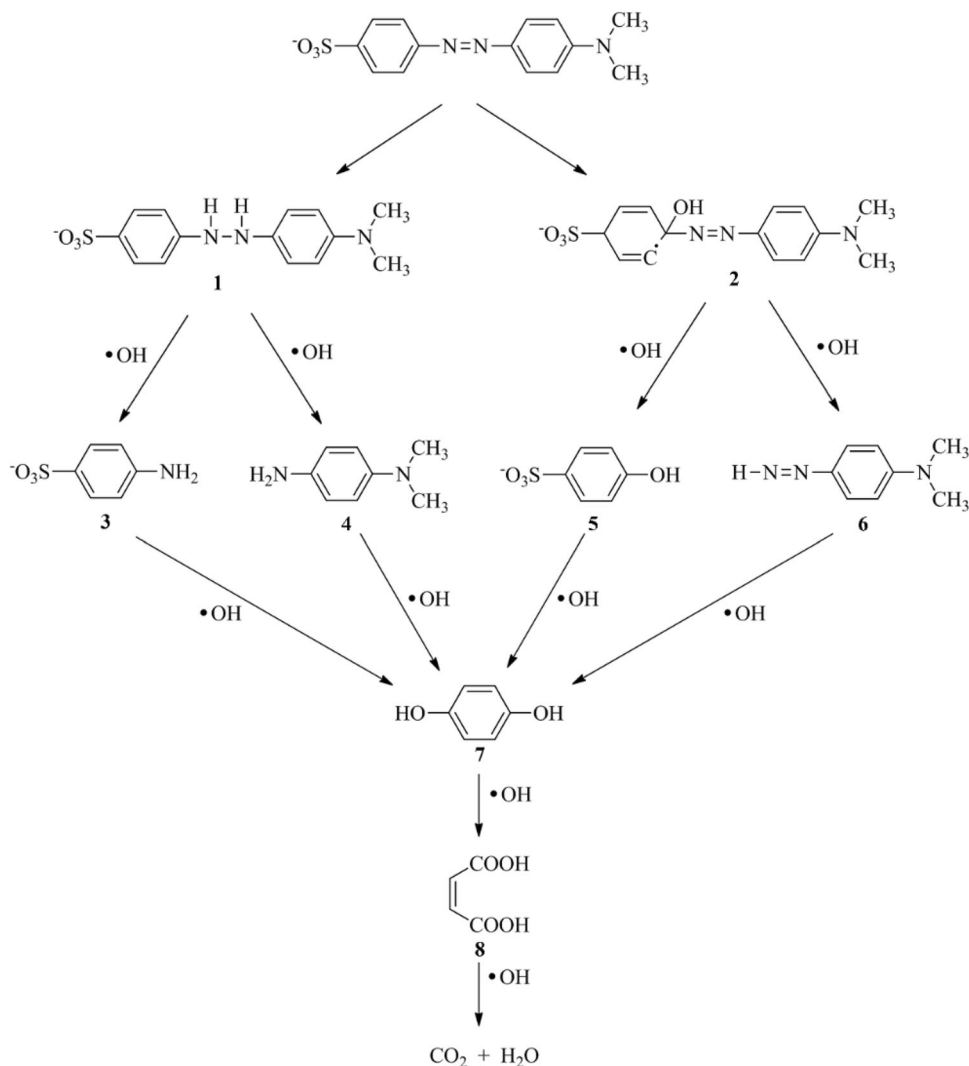
198, 182, and 149 were shown in Fig. S14 at 60 min, corresponding to C₆H₇O₄SNa, C₆H₇O₃SNa, and C₈H₁₁N₃, respectively. Based on these analysis, the main degradation products are summarized in Table 1, and the probable photocatalytic degradation mechanism of MO is shown in Fig. 6.

Considering the possibility of electron transfer, the degradation mechanism was proposed as follows:

Table 1 Main degradation products of MO

Molecular weight	Structure
327	
306	
175	
149	
110	
116	

Fig. 6 The degradation mechanism of MO



Firstly, the quinoid structure in MO was oxidized to generate compounds 1 and 2 under acidic conditions. The N–N bond of compound 1 was broken due to the attack of the active group $\cdot\text{OH}$, and compounds 3 and 4 were generated. The compound 2 was oxidized by the attack of $\cdot\text{OH}$ to form the compounds 5 and 6. The N–C bond connected with the benzene ring in the compounds 3, 4, and 6 was broken due to the attack of the active group $\cdot\text{OH}$, leading to the formation of the compound 7. Meanwhile, the $\text{O}_3\text{S}-\text{C}$ bond connected with the benzene ring of the compounds 3 and 5 was fractured and oxidized to generate the compound 7. Subsequently, the benzene ring of compound 7 was further fractured and oxidized to generate the compound 8. These intermediate products could be further oxidized to CO_2 and H_2O in the end.

The schematic representation of the energy band structure, electron–hole pair separation, and reaction mechanism for $\text{p-CaFe}_2\text{O}_4/\text{n-Fe}_2\text{O}_3$ is shown in Fig. 7. Since the built-in electric potential in the space charge region, the excited electrons on the $\text{p-CaFe}_2\text{O}_4$ would be transferred to that of $\text{n-Fe}_2\text{O}_3$, and the holes produced by $\text{n-Fe}_2\text{O}_3$ are injected into the $\text{p-CaFe}_2\text{O}_4$, resulting in the effective separation of photoelectrons and holes. Therefore, the electrons of $\text{n-Fe}_2\text{O}_3$ could react with H_2O_2 to form $\cdot\text{OH}$, and the $\text{OH}^-/\text{H}_2\text{O}$ could be oxidized by the holes of $\text{p-CaFe}_2\text{O}_4$ to product active species $\cdot\text{OH}$ in the photocatalytic reaction (Eqs. 8–10). The active species $\cdot\text{OH}$ could promote the degradation of MO (Eq. 11).



Fig. 7 The schematic representation of the energy band structure, electron–hole pair separation, and reaction mechanism for p-CaFe₂O₄/n-Fe₂O₃

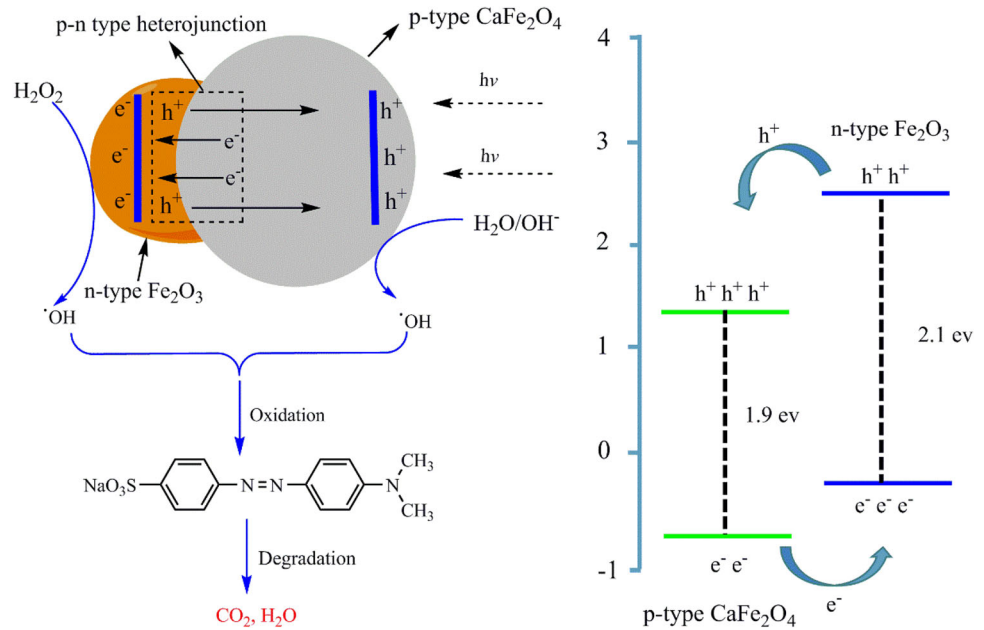
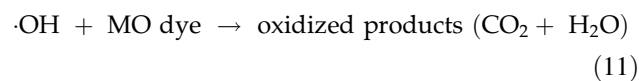


Table 2 Comparison of photocatalytic performance for removal of MO with other studies

Samples	C (mg/L)	Time (min)	Degradation rate (%)	Refs.
TiO ₂ /FeOOH	20	180	80	[44]
Fe ₂ O ₃ /TiO ₂	10	25	88	[45]
TiO ₂ /MoS ₂ @zeolite	20	60	95	[46]
ZnO/ZnS	20	120	95	[47]
g-C ₃ N ₄ /ZnS	10	100	93.0	[48]
p-CaFe ₂ O ₄ /n-Fe ₂ O ₃	50	60	99	This work



3.6 Comparison with other studies

Table 2 compares the photocatalytic performance of p-CaFe₂O₄/n-Fe₂O₃ with other common composite photocatalysts for the degradation of MO. It can be clearly seen that the p-CaFe₂O₄/n-Fe₂O₃ in this work exhibited excellent catalytic efficiency for MO removal. We can believe that the photocatalyst will be a good candidate for applications in organic pollutants removal from wastewater.

4 Conclusions

In this study, we designed a new p-CaFe₂O₄/n-Fe₂O₃ nanocomposite with p–n heterojunction to improve the MO degradation rate. The mass ratio of n-Fe₂O₃ and p-CaFe₂O₄, dosage of composite photocatalyst, volume of H₂O₂, the initial concentration of MO, and pH value of MO degradation in the H₂O₂/UV system were chosen as 1:1.25, 10 mg, 30 μL, 50 mg/L, and 6.5, respectively, and the degradation rate can reach 99% at 60 min under the above optimum conditions. Meanwhile, the prepared sample showed high removal ability after 5th cycle. Furthermore, degradation intermediates including C₁₄H₁₆N₃O₃S-, C₆H₇O₄S-, C₈H₁₁N₃, C₆H₆O₂, and C₄H₄O₄ and so on were identified, and a possible degradation pathway of MO was proposed. The MO degradation enhancement can be attributed to the construction of the heterojunction in composite material, which reduces the photocatalytic photoelectron–hole recombination and generates more hydroxyl radicals

for the MO oxidation. All in all, p-CaFe₂O₄/n-Fe₂O₃ composite is a new p–n-type photocatalyst to be applied in the field of MO degradation, and the results and the mechanism presented in this study will provide theory reference for the exploration of more effective photocatalysts applied in the wastewater degradation treatment.

Acknowledgements

The authors are grateful to Fundamental Research Funds for the Central Universities (N180506002 and N180705004).

Electronic supplementary material: The online version of this article (<https://doi.org/10.1007/s10854-020-04349-9>) contains supplementary material, which is available to authorized users.

References

- N.M. Mahmoodi, J. Abdi, M. Oveisi, M.A. Asli, M. Vosoughi, *Mater. Res. Bull.* **100**, 357 (2018)
- Y.N. Rane, D.A. Shende, M.G. Raghuvanshi, R.R. Koli, S.R. Gosavi, N.G. Deshpande, *Optik* **179**, 535 (2019)
- S. Ahmed, M.G. Rasul, W.N. Martens, R. Brown, M.A. Hashib, *Desalination* **261**, 3 (2010)
- R. Khan, M.S. Hassan, H.S. Cho, A.Y. Polyakov, M.S. Khil, I.H. Lee, *Mater. Lett.* **133**, 224 (2014)
- N. Daneshvar, S. Aber, A. Khani, A.R. Khataee, *J. Hazard. Mater.* **144**, 47 (2007)
- A. Alinsafi, M. Khemis, M.N. Pons, J.P. Leclerc, A. Yaacoubi, A. Benhammou, A. Nejmeddine, *Chem. Eng. Process.* **44**, 461 (2005)
- P.V.A. Padmanabhan, K.P. Sreekumar, T.K. Thiyagarajan, R.U. Satpute, K. Bhanumurthy, P. Sengupta, G.K. Dey, K.G.K. Warriar, *Vacuum* **80**, 1252 (2006)
- H. Dong, I.M. Lo, *Water Air Soil Poll.* **225**, 2107 (2014)
- F. Petronella, A. Truppi, C. Ingrosso, T. Placido, M. Striccoli, M.L. Curri, A. Agostiano, R. Comparelli, *Catal. Today* **281**, 85 (2017)
- M. Hojamberdiev, Z.C. Kadirova, Y. Makinose, G. Zhu, S. Emin, N. Matsushita, M. Hasegawa, K. Okada, *Colloids Surf. A* **529**, 600 (2017)
- Z. Barzgari, S.Z. Askari, A. Ghazizadeh, *J. Mater. Sci. Mater. Electron.* **28**, 1 (2017)
- H. Chaker, L. Chérif-Aouali, S. Khaoulani, A. Bengueddach, S. Fourmentin, *J. Photochem. Photobiol. A* **142**, 318 (2016)
- C. Andriantsiferana, E.F. Mohamed, H. Delmas, *Environ. Technol.* **3**, 355 (2014)
- C.B.D. Marien, T. Cottineau, D. Robert, P. Drogui, *Appl. Catal. B* **194**, 1 (2016)
- S.J. Hong, H. Jun, P.H. Borse, J.S. Lee, *Int. J. Hydrog. Energy* **34**, 3234 (2009)
- C. Yang, J. Yu, Q. Li, Y. Yu, *Mater. Res. Bull.* **87**, 72 (2017)
- M. Pelaez, N.T. Nolan, S.C. Pillai, M.K. Seery, P. Falaras, A.G. Kontos, P.S.M. Dunlop, J.W.J. Hamilton, J.A. Byrne, K.O. Shea, M.H. Entezari, D.D. Dionysiou, *Appl. Catal. B* **125**, 331 (2012)
- Z. Zhang, C. Shao, X. Li, C. Wang, M. Zhang, Y. Liu, A.C.S. *Appl. Mater. Interfaces* **2**, 2915 (2010)
- J. Hu, Z. Zhong, F. Zhang, W. Xing, W. Jin, N. Xu, *Ind. Eng. Chem. Res.* **55**, 6661 (2016)
- Y.T. Song, L.Y. Lin, Y.S. Chen, H.Q. Chen, Z.D. Ni, C.C. Tu, S.S. Yang, *RSC Adv.* **6**, 49130 (2016)
- D. Sarkar, G.G. Khan, A.K. Singh, K. Mandal, *J. Phys. Chem. C* **116**, 23540 (2012)
- Y. Zhang, Y. Yu, X. Wang, G. Tong, L. Mi, X. Geng, *J. Mater. Chem. C* **5**, 140 (2017)
- Q. Liang, J. Jin, M. Zhang, C. Liu, S. Xu, C. Yao, Z. Li, *Appl. Catal. B* **218**, 545 (2017)
- M. Tyagi, M. Tomar, V. Gupta, *J. Mater. Chem. C* **2**, 2387 (2014)
- Q. Liang, J. Jin, C. Liu, S. Xu, Z. Li, *J. Alloy. Compd.* **709**, 542 (2017)
- Y. Fu, Y. Li, J. Hu, S. Li, G. Qin, *Optik* **178**, 36 (2019)
- A. Umar, M. Abaker, M. Faisal, S.W. Hwang, S. Baskoutas, S.A. Al-Sayari, *J. Nanosci. Nanotechnol.* **4**, 3474 (2011)
- H. Zhang, H. Ming, S. Lian, H. Huang, H. Li, L. Zhang, Y. Liu, Z. Kang, S.T. Lee, *Dalton Trans.* **40**, 10822 (2011)
- P. Sharma, R. Kumar, S. Chauhan, D. Singh, M.S. Chauhan, *J. Nanosci. Nanotechnol.* **8**, 6153 (2014)
- S.A. Jadhav, S.B. Somvanshi, M.V. Khedkar, S.R. Patade, K.M. Jadhav, *J. Mater. Sci. Mater. Electron.* **31**, 11352 (2020)
- A.V. Humbe, J.S. Kounsalye, S.B. Somvanshi, A. Kumar, K.M. Jadhav, *Mater. Adv.* **1**, 880 (2020)
- S.B. Somvanshi, S.R. Patade, D.D. Andhare, S.A. Jadhav, M.V. Khedkar, P.B. Kharat, P.P. Khirade, K. Jadhav, *J. Alloys Compd.* **835**, 155422 (2020)
- X. Liu, Y. Zhang, Y. Jia, J. Jiang, Y. Wang, X. Chen, T. Gui, *Chin. J. Catal.* **38**, 1770 (2017)
- Z. Zhang, W. Wang, *Mater. Lett.* **133**, 212 (2014)
- S. Ida, K. Yamada, H. Hagiwara, T. Ishihara, *J. Phys. Chem.* **72**, 1682 (2011)
- M. Goodarzi, S. Joukar, D. Ghanbari, K. Hedayati, *J. Mater. Sci. Mater. Electron.* **28**, 1 (2017)

37. E.S. Kim, N. Nishimura, G. Magesh, J.Y. Kim, J.W. Jang, H. Jun, J. Kubota, K. Domen, J.S. Lee, *J. Am. Chem. Soc.* **135**, 5375 (2013)
38. H.G. Kim, P.H. Borse, J.S. Jang, E.D. Jeong, O.S. Jung, Y.J. Suh, J.S. Lee, *Chem. Commun.* **41**, 5889 (2010)
39. M. Saquiba, M. Abu Tariqa, M.M. Haquea, M. Muneer, *J. Environ. Manag.* **88**, 300 (2008)
40. Q. Zhang, C.L. Li, T. Li, *Chem. Eng. J.* **217**, 407 (2013)
41. W.H. Chu, N.Y. Gao, Y. Deng, *Clean-Soil Air Water* **37**, 233 (2009)
42. Z. Eren, *Acta Hydrochem. Hydrobiol.* **40**, 1284 (2012)
43. M. Huang, C. Xu, Z. Wu, Y. Huang, J. Lin, J. Wu, *Dyes Pigments* **77**, 327 (2008)
44. D. Chen, S.J. Hu, G.H. Li, *Adv. Mater. Res.* **535**, 219 (2012)
45. L. Wu, H. Yan, J. Xiao, X. Li, X. Wang, T. Zhao, *Ceram. Int.* **43**, 14334 (2017)
46. W. Zhang, X. Xiao, L. Zheng, C. Wan, *Appl. Surf. Sci.* **358**, 468 (2015)
47. W. Li, G. Song, F. Xie, M. Chen, Y. Zhao, *Mater. Lett.* **96**, 221 (2013)
48. Q. Wang, Y. Shi, Z. Du, J. He, J. Zhong, L. Zhao, H. She, G. Liu, B. Su, *Eur. J. Inorg. Chem.* **2015**, 4108 (2015)

Publisher's Note Springer Nature remains neutral with regard to jurisdictional claims in published maps and institutional affiliations.